

Accelerated Article Preview**Multiple pathways for SARS-CoV-2 resistance to nirmatrelvir**

Received: 6 July 2022

Accepted: 2 November 2022

Accelerated Article Preview

Cite this article as: Iketani, S. et al. Multiple pathways for SARS-CoV-2 resistance to nirmatrelvir. *Nature* <https://doi.org/10.1038/s41586-022-05514-2> (2022)

Sho Iketani, Hiroshi Mohri, Bruce Culbertson, Seo Jung Hong, Yinkai Duan, Maria I. Luck, Medini K. Annavajhala, Yicheng Guo, Zizhang Sheng, Anne-Catrin Uhlemann, Stephen P. Goff, Yosef Sabo, Haitao Yang, Alejandro Chavez & David D. Ho

This is a PDF file of a peer-reviewed paper that has been accepted for publication. Although unedited, the content has been subjected to preliminary formatting. Nature is providing this early version of the typeset paper as a service to our authors and readers. The text and figures will undergo copyediting and a proof review before the paper is published in its final form. Please note that during the production process errors may be discovered which could affect the content, and all legal disclaimers apply.

Multiple pathways for SARS-CoV-2 resistance to nirmatrelvir

1 Sho Iketani^{1,2*}, Hiroshi Mohri^{1,2*}, Bruce Culbertson^{3,4*}, Seo Jung Hong^{5*}, Yinkai Duan⁶, Maria
2 I. Luck^{1,2}, Medini K. Annavajhala², Yicheng Guo^{1,2}, Zizhang Sheng^{1,2}, Anne-Catrin Uhlemann²,
3 Stephen P. Goff^{1,7,8}, Yosef Sabo^{1,2}, Haitao Yang⁶, Alejandro Chavez^{5^}, David D. Ho^{1,2,7^}

4
5 ¹ Aaron Diamond AIDS Research Center, Columbia University Vagelos College of Physicians
6 and Surgeons, New York, NY, USA

7 ² Division of Infectious Diseases, Department of Medicine, Columbia University Vagelos College
8 of Physicians and Surgeons, New York, NY, USA

9 ³ Integrated Program in Cellular, Molecular, and Biomedical Studies, Columbia University
10 Vagelos College of Physicians and Surgeons, New York, NY, USA

11 ⁴ Medical Scientist Training Program, Columbia University Vagelos College of Physicians and
12 Surgeons, New York, NY, USA

13 ⁵ Department of Pathology and Cell Biology, Columbia University Vagelos College of Physicians
14 and Surgeons, New York, NY, USA

15 ⁶ Shanghai Institute for Advanced Immunochemical Studies and School of Life Science and
16 Technology, ShanghaiTech University, Shanghai, China

17 ⁷ Department of Microbiology and Immunology, Columbia University Vagelos College of
18 Physicians and Surgeons, New York, NY, USA

19 ⁸ Department of Biochemistry and Molecular Biophysics, Columbia University Vagelos College
20 of Physicians and Surgeons, New York, NY, USA

21
22 * These authors contributed equally

23 ^ Address correspondence to Alejandro Chavez (ac4304@cumc.columbia.edu) and David D. Ho
24 (dh2994@cumc.columbia.edu, 212-304-6101, 701 W 168th St, 11th Floor, New York, NY
25 10032)

26
27 Word count: 3128

28 **Abstract**

29

30 Nirmatrelvir, an oral antiviral targeting the 3CL protease of SARS-CoV-2, has been demonstrated
31 to be clinically useful against COVID-19^{1,2}. However, as SARS-CoV-2 has evolved to become
32 resistant to other therapeutic modalities³⁻⁹, there is a concern that the same could occur for
33 nirmatrelvir. Here, we have examined this possibility by *in vitro* passaging of SARS-CoV-2 in
34 nirmatrelvir using two independent approaches, including one on a large scale. Indeed, highly
35 resistant viruses emerged from both, and their sequences revealed a multitude of 3CL protease
36 mutations. In the experiment done with many replicates, 53 independent viral lineages were
37 selected with mutations observed at 23 different residues of the enzyme. Yet, several common
38 mutational pathways to nirmatrelvir resistance were preferred, with a majority of the viruses
39 descending from T21I, P252L, or T304I as precursor mutations. Construction and analysis of 13
40 recombinant SARS-CoV-2 clones showed that these mutations only mediated low-level resistance,
41 whereas greater resistance required accumulation of additional mutations. E166V mutation
42 conferred the strongest resistance (~100-fold), but this mutation resulted in a loss of viral
43 replicative fitness that was restored by compensatory changes such as L50F and T21I. Our findings
44 indicate that SARS-CoV-2 resistance to nirmatrelvir does readily arise via multiple pathways *in*
45 *vitro*, and the specific mutations observed herein form a strong foundation from which to study the
46 mechanism of resistance in detail and to inform the design of next generation protease inhibitors.

47

48 **Main text**

49 The COVID-19 (coronavirus disease 2019) pandemic has continued to affect the global populace.
50 The rapid development and deployment of effective vaccines as well as monoclonal antibody
51 therapeutics beginning in late 2020 have helped to greatly curtail its impacts¹⁰⁻¹⁶. Yet, the etiologic
52 agent, SARS-CoV-2 (severe acute respiratory syndrome coronavirus 2), has continuously evolved
53 to develop resistance to antibody-mediated neutralization⁴⁻⁸. In particular, several of the recent
54 Omicron subvariants exhibit such strong antibody resistance that vaccines have had their
55 protection against infection dampened and a majority of current monoclonal therapeutics have lost
56 efficacy^{4,5,8}, as manifested by increasing breakthrough infections in convalescing and/or
57 vaccinated individuals³.

58
59 Fortunately, treatment options remain. In the United States, three antivirals have received
60 emergency use authorization for COVID-19 treatment: remdesivir^{17,18}, molnupiravir¹⁹⁻²¹, and
61 nirmatrelvir^{1,2} (also known as PF-07321332, used in combination with ritonavir and marketed as
62 PAXLOVID™). The first two target the RNA-dependent RNA polymerase (RdRp), and the latter
63 targets the 3CL protease (3CL^{pro}; also known as main protease (M^{pro}) and nonstructural protein 5
64 (nsp5)). Both enzymes are essential for the viral life cycle and relatively conserved among
65 coronaviruses^{22,23}. Remdesivir is administered intravenously and has a reported relative risk
66 reduction of 87%¹⁸, whereas molnupiravir and nirmatrelvir are administered orally and have
67 reported clinical efficacies of 31%²⁰ and 89%¹, respectively, in lowering hospitalization or death.
68 As the use of these antivirals increases, there is a concern that drug resistance may arise,
69 particularly if given as monotherapies. For remdesivir, *in vitro* and *in vivo* studies have revealed
70 mutations associated with resistance^{9,24,25}, and resistance to molnupiravir or nirmatrelvir is now
71 under active investigation. Here, we report that there are multiple routes by which SARS-CoV-2
72 can gain resistance to nirmatrelvir *in vitro*.

73
74 **Nirmatrelvir resistance in Vero E6**

75 To select for resistance to nirmatrelvir, SARS-CoV-2 (USA-WA1/2020 strain) was passaged in
76 the presence of increasing concentrations of the drug (see **Methods** for details). We conducted this
77 initial experiment in triplicate, using Vero E6 cells as they have been one of the standard cell lines
78 used in COVID-19 research. After 30 passages, each of the three lineages demonstrated a high

79 level of resistance, with IC₅₀ values increasing 33- to 50-fold relative to that of the original virus
80 (**Figs. 1a-d**). Examination of earlier viral passages confirmed a stepwise increase in nirmatrelvir
81 resistance with successive passaging (**Figs. 1b-d**), without any evidence of resistance to remdesivir
82 (**Fig. 1e**). The resistant viruses selected by passaging maintained their replicative fitness *in vitro*,
83 with similar growth kinetics as those passaged without nirmatrelvir (**Extended Data Fig. 1**).

84
85 We then sequenced the 3CL^{pro} gene from the three viral lineages collected every three passages to
86 investigate which mutations may confer resistance (**Fig. 1f**). We found that the three lineages
87 harbored unique mutations, with only one mutation, at most, overlapping between the different
88 lineages (T21I in lineages A and B, L50F in lineages B and C, and T304I in lineages A and C).
89 The observed mutations occurred in a stepwise manner, mirroring the increases in drug resistance
90 (**Fig. 1f**), and a number of them, but not all, were situated near the nirmatrelvir-binding site (**Fig.**
91 **1g**). Specifically, F140L and L167F were within 5 Å from nirmatrelvir. These results suggested
92 that SARS-CoV-2 could readily develop nirmatrelvir resistance using several mutational pathways.

93 94 **Nirmatrelvir resistance in Huh7-ACE2**

95 We therefore set out to conduct another passaging experiment to select for nirmatrelvir resistance,
96 but this time at a larger scale with many replicates to better capture the multitude of solutions that
97 SARS-CoV-2 could adopt under drug pressure. For these later studies, we utilized Huh7-ACE2
98 cells to examine if differences would arise in human cells, and because Vero E6 cells express high
99 levels of P-glycoprotein, an efflux transporter that limits the intracellular accumulation of
100 nirmatrelvir²⁶. We passaged SARS-CoV-2-mNeonGreen (USA-WA1/2020 background with
101 ORF7 replaced with mNeonGreen²⁷) independently in 480 wells for 16 passages, with increasing
102 concentrations of nirmatrelvir over time, and viruses from every fourth passage were subjected to
103 next-generation sequencing (NGS) (**Fig. 2a** and see **Methods** for details). After 16 passages,
104 varying degrees of nirmatrelvir resistance were observed as exemplified by the three viruses shown
105 (**Fig. 2b**). Sequencing of the 3CL^{pro} in all wells that retained mNeonGreen signal identified 53
106 mutant populations (**Fig. 2c**). Across all of these populations, mutations were observed at 23
107 residues within the enzyme (1-6 mutations in each isolate), both proximal (≤ 5 Å; S144A,
108 E166(A/V), H172(Q/Y), and R188G) and distal (> 5 Å) to nirmatrelvir (**Fig. 2d**). While there was
109 widespread diversity among the passaged populations, seven mutations appeared ten or more times

110 across replicates: T21I, L50F, S144A, E166V, A173V, P252L, and T304I. The only frequently
111 observed 3CL^{pro} cleavage site mutation is T304I, which corresponds to the cleavage site nsp5/6
112 T(P3)I. Other sites were only rarely observed to mutate, suggesting that substrate cleavage site
113 alterations are largely not responsible for the nirmatrelvir resistance (**Extended Data Fig. 2**), with
114 the possible exception of cis-cleavage.

115
116 Sequencing of the same wells at earlier passages revealed less diversity in 3CL^{pro}, with a total of
117 11, 16, and 22 unique mutations detected across all populations from passages 4, 8, and 12,
118 respectively (**Supplemental Table 1**). As a standard phylogenetic analysis showed a rather
119 complex stepwise order of acquisition of mutations for each passaged lineage (**Fig. 3a**), we more
120 carefully analyzed the order in which mutations arose across the various lineages (see **Methods**
121 and **Supplemental Table 1** for details) and generated a pathway network delineating the most
122 common routes that SARS-CoV-2 took *in vitro* to develop nirmatrelvir resistance (**Fig. 3b and**
123 **Supplemental Table 2**). The majority of these viral lineages descended initially from T21I, P252L,
124 and T304I, suggesting that these mutations may serve as “founder” or “precursor” mutations when
125 the drug concentrations are relatively low. Additional mutations then occurred, probably to
126 increase the level of resistance as the drug concentrations were increased and/or to compensate for
127 reduced viral fitness. These findings indicated that although there are multiple solutions for SARS-
128 CoV-2 to resist nirmatrelvir, several common mutational pathways are favored.

129

130 **Nirmatrelvir resistance mutations**

131 To further investigate which mutations were responsible for nirmatrelvir resistance, we proceeded
132 to generate recombinant SARS-CoV-2 clones, each containing a unique mutation or a combination
133 of mutations. To construct the 15 mutant viruses from the first passage experiment (**Fig. 1f**) and
134 the 22 mutant viruses from the second passage experiment (**Fig. 3a, b**) would be beyond the scope
135 of the current study. We therefore decided to focus on the seven most common single point mutants
136 from the large passaging study, as well as five double mutants and one triple mutant (**Extended**
137 **Data Fig. 3**). All viruses grew similarly to wild type (WT) in the absence of drug, except for
138 S144A, E166V, and T21I + S144A, which were significantly impaired in their growth kinetics
139 (**Fig. 3c**). However, both T21I + E166V and L50F + E166V replicated well with kinetics similar
140 to WT, suggesting that T21I and L50F each compensated for the fitness loss of E166V. Of the

141 individual mutants tested against nirmatrelvir, E166V was most resistant (100-fold), with P252L
142 and T304I having low-level resistance (~6-fold), and S144A and A173V having minimal
143 resistance (~3-fold or less) (**Figs. 4a, 4b and Extended Data Fig. 4**). Combination of either T21I
144 or L50F with E166V resulted in a virus that was substantially resistant to nirmatrelvir (83-fold and
145 53-fold, respectively), but with WT replicative kinetics (**Fig. 3c**).

146

147 We next tested this panel of viruses against ensitrelvir²⁸ (also known as S-217622), another 3CL
148 protease inhibitor that has demonstrated clinical efficacy²⁹, for cross-resistance together with
149 remdesivir as a control. Only S144A, E166V, and T21I + S144A showed substantial (13 to 23-
150 fold) cross-resistance to ensitrelvir (**Fig. 4b and Extended Data Figs. 4, 5**). As expected, none of
151 these mutations conferred resistance to remdesivir. We additionally tested the passage 30 viruses
152 resulting from the initial selection experiment in Vero E6 cells (**Fig. 1**) against these two inhibitors.
153 Again, all three lineages were as susceptible to remdesivir as WT, and only lineage C (L50F +
154 F140L + L167F + T304I) showed cross-resistance to ensitrelvir (~25-fold) (**Extended Data Fig.**
155 **6**). This may be due to F140L, since L50F and T304I did not demonstrate ensitrelvir resistance
156 (**Fig. 4b**) and L167 does not contact ensitrelvir (see below). Together, these results suggest that
157 some mutations, such as E166V, can confer a high degree of nirmatrelvir resistance alone, while
158 others, such as T21I, P252L, and T304I, confer only low levels of nirmatrelvir resistance
159 individually. The degree of cross-resistance to ensitrelvir was variable among the tested mutant
160 viruses probably due to the differences in binding of these drugs to the substrate binding site of
161 3CL^{pro} (**Extended Data Fig. 7a**). Nevertheless, it is clear that selection for nirmatrelvir resistance
162 can yield mutations that confer cross-resistance to other inhibitors of clinical interest as well.

163

164 To begin to understand the mechanisms underlying the resistance conferred by these mutations,
165 we considered their structural context. Nirmatrelvir and ensitrelvir both bind within the substrate
166 binding site, but in differing modes, which may result in the differences observed in the inhibition
167 profiles of the mutants (**Figs. 4b and Extended Data Fig. 7a**). E166 directly interacts with the
168 lactam ring of nirmatrelvir via hydrogen bonding, and the valine substitution at this position may
169 abrogate some of these interactions to result in the strong drug resistance observed (**Extended**
170 **Data Fig. 7b**). E166 is also able to form hydrogen bonds with the first residue (S1) of the
171 neighboring protomer and therefore is involved in dimerization, which is essential for protease

172 activity as the 3CL^{pro} functions as a homodimer³⁰. The disruption of the hydrogen-bonding
173 interactions (**Extended Data Fig. 7b**) may explain the reduced fitness of the E166V mutant (**Fig.**
174 **3c**). The side chain of S144 forms a hydrogen bond with the main chain of L141 to stabilize the
175 S1 subsite of the substrate binding site, so the S144A mutation may disorder this region and
176 hamper the binding of both nirmatrelvir and ensitrelvir (**Extended Data Fig. 7c**), although it is not
177 clear why this requires the T21I mutation in conjunction. L167 participates in the formation of the
178 S4 subsite, and the L167F mutation may cause a steric clash with nirmatrelvir (**Extended Data**
179 **Fig. 7d**). However, as ensitrelvir does not extend into the S4 subsite, this mutation may not be
180 responsible for the cross-resistance observed in lineage C (**Extended Data Fig. 6**). As F140
181 interacts by π - π stacking interactions with H163, which directly interacts with both nirmatrelvir
182 and ensitrelvir, the F140L mutation may abrogate this interaction, resulting in resistance
183 (**Extended Data Fig. 6, 7a, 7b**). For a number of these mutations, however, it is not immediately
184 apparent how they confer drug resistance given that they are distant from the substrate binding site
185 where the drugs bind (**Extended Data Fig. 3**).

186
187 Finally, we compared the mutations identified in this study to clinical SARS-CoV-2 sequences
188 reported to GISAID³¹. Nearly all of the mutations we have identified were observed among the
189 viruses circulating in the population, albeit at low frequencies (**Extended Data Fig. 8a**).
190 Comparing the frequencies of these mutations in periods before and after the authorization of the
191 combination of nirmatrelvir and ritonavir (PAXLOVIDTM) did not show an appreciable increase
192 in the observed mutations (**Extended Data Fig. 8b**).

193
194 **Discussion**
195 As antibody-based interventions for SARS-CoV-2 face increasing resistance by the emergence of
196 variants of concern, antivirals with alternative modes of action have increased in importance.
197 Nirmatrelvir, as an oral antiviral targeting 3CL^{pro}, is a therapeutic that has shown high efficacy in
198 lowering severe disease and hospitalization in infected persons who are at high risk and not
199 vaccinated^{1,2}. Indeed, it is the most commonly used antiviral drug to treat COVID-19 today³².
200 Given the adaptations that the virus has already exhibited to other modes of treatment³⁻⁹, it is
201 clinically important to understand the mechanisms by which nirmatrelvir resistance can occur. The
202 results presented herein demonstrate that *in vitro* high-level resistance to nirmatrelvir can be

203 readily achieved by SARS-CoV-2, and that this can occur in a multitude of ways. This finding is
204 consistent with our prior report on the extensive plasticity of the 3CL^{pro} as discovered by deep
205 mutational scanning³³.

206

207 In both Vero E6 cells (**Fig. 1**) and Huh7-ACE2 cells (**Fig. 2**), multiple lineages with non-
208 overlapping mutations evolved under increasing drug pressure, consistent with what has been seen
209 in similar small-scale studies^{24,25,34,35}. Conducting selection at scale, however, revealed that there
210 are multiple mutational pathways to nirmatrelvir resistance but with several common trajectories
211 preferred (**Figs. 2c, 3a, 3b**). A majority of lineages descended from viruses that acquired T21I,
212 P252L, or T304I as an initial mutation. Recombinant SARS-CoV-2 constructed to contain each of
213 these point mutants exhibited low-level resistance (**Figs. 4a, 4b**), suggesting that each of these
214 precursor mutations may have allowed the virus to tolerate low concentrations of nirmatrelvir but
215 required additional mutations as the drug pressure was increased. Notably, all three of these
216 mutations are rather distal ($> 5 \text{ \AA}$) from nirmatrelvir (**Fig. 2d**), and their mechanism for resistance
217 is not evident without additional studies. We note, however, that T304 corresponds to the P3 site
218 on the nsp5/6 cleavage substrate for 3CL^{pro} of both SARS-CoV and SARS-CoV-2 (**Extended Data**
219 **Fig. 2**). Although the P3 site is exposed to solvent and thus not considered to confer stringent
220 substrate specificity, it has been shown that a suitable functional group (such as the side chain of
221 isoleucine) at the P3 site can assist in increasing inhibitor/substrate potency and selectivity for
222 3CL^{pro}s³⁶⁻³⁸. Therefore, it is possible that T304I could facilitate the binding of the nsp5/6 cleavage
223 site or promote the autocleavage process. The differing mutations observed between the two cell
224 lines further emphasize the complexity and variety of pathways to achieve nirmatrelvir resistance,
225 although it is not yet clear why certain mutations were specific to the Vero E6 cell line.

226

227 Analyses with isogenic mutants also revealed that several mutations are responsible for the
228 observed nirmatrelvir resistance, with the E166V mutation conferring the most resistance (100-
229 fold) (**Fig. 4b**), as is being reported elsewhere^{33,35}. This mutation, as well, conferred a degree of
230 cross-resistance to ensitrelvir, another clinically relevant 3CL^{pro} inhibitor^{28,29}. The mechanism of
231 resistance of E166V is explainable since it resides in the substrate binding site, and the valine
232 substitution disrupts its hydrogen bonding to the lactam ring of nirmatrelvir (**Extended Data Fig.**
233 **7b**). However, this mutation lowered the replicative fitness of the virus in vitro (**Fig. 3c**), perhaps

234 because of a loss of interaction with the first residue of the neighboring protomer in dimerization
235 (**Extended Data Fig. 7b**)³⁰. Importantly, replicative fitness was restored when T21I or L50F was
236 added (**Fig. 3c**), without a significant impact on drug resistance (**Fig. 4b**). How these two mutations
237 compensate for the fitness loss of E166V remains unknown. It is worth mentioning that the E166V
238 mutation was reported to be found in viral isolates from a few of the PAXLOVID™-treated
239 individuals in the EPIC-HR clinical trial¹ (see Fact Sheet for Healthcare Providers: Emergency
240 Use Authorization for PAXLOVID™, revised July 6, 2022).

241
242 We have also found that a number of additional mutations could confer resistance to nirmatrelvir
243 *in vitro*. T21I + S144A mediated not only significant resistance to nirmatrelvir but also cross-
244 resistance to ensitrelvir (**Fig. 4b**), but this virus exhibited slower growth kinetics (**Fig. 3c**).
245 Likewise, we inferred that both L167F and F140L were likely mediating drug resistance in the C-
246 P30 lineage of the first *in vitro* passaging experiment (**Fig. 1f**) as discussed above along with
247 possible structural explanations. It is clear, nevertheless, that we have only studied a limited
248 number of the mutational pathways that SARS-CoV-2 took to evade nirmatrelvir. Furthermore,
249 many of the mutations revealed by our study are without a straightforward structural explanation
250 at this time, and indeed, while other *in vitro* or *in silico* studies have identified residues such as
251 E166 to be of importance, they have missed these other residues that are distant from the substrate
252 binding site³⁹⁻⁴¹. It should also be mentioned that our studies were conducted with the ancestral
253 WA1 strain, and the currently circulating Omicron variants, all of which except for BA.3 contain
254 a P132H mutation in 3CL^{pro}, may differ in their nirmatrelvir evasion pathways. While this mutation
255 has been reported to have no direct effect on nirmatrelvir resistance, it may influence the
256 emergence of subsequent resistance conferring mutations⁴². It will require extensive virological,
257 biochemical, and structural studies to delineate which mutations confer resistance and how, as well
258 as to understand how certain mutations play compensatory roles. A better understanding of the
259 mechanisms of nirmatrelvir resistance could provide insight into the development of the next
260 generation of 3CL^{pro} inhibitors.

261
262 Nirmatrelvir has been used to treat COVID-19 for only 6 months or less in most countries. SARS-
263 CoV-2 resistance to this drug in patients has yet to be reported, and we see no appreciable
264 difference in frequencies of the 3CL^{pro} mutations that we have uncovered in periods before and

265 after the emergency use authorization (**Extended Data Fig. 8**). Perhaps the lack of nirmatrelvir
266 resistance in patients to date is due to the high drug concentrations achieved with the prescribed
267 regimen, making it difficult for the virus to accumulate mutations in a stepwise manner. In addition,
268 the drug is administered while the immune system is also actively eliminating the virus, including
269 any resistant forms that may have emerged. Therefore, it makes sense to focus our surveillance
270 effort on immunocompromised individuals on nirmatrelvir treatment for the appearance of drug-
271 resistant virus. Past experience with other viral infections tells us that if drug resistance could be
272 selected *in vitro*, it surely will occur *in vivo*. Although current COVID-19 therapies have been
273 largely administered as monotherapies, it is possible that future treatment will benefit from the use
274 of a combination of drugs to minimize the likelihood of SARS-CoV-2 escape.

275

276 **Figure Legends**

277

278 **Fig. 1. Identification of nirmatrelvir resistance in Vero E6 cells.** **a**, Changes in IC_{50} during
279 passaging of SARS-CoV-2 with nirmatrelvir. Vero E6 cells were infected in triplicate with SARS-
280 CoV-2 (USA-WA1/2020) and passaged to fresh cells every 3 days for 30 passages. See Methods
281 for additional details. **b-d**, Validation of nirmatrelvir resistance from the indicated passage from
282 each of the three lineages, A, B, and C, respectively. **e**, Inhibition of passage 30 viruses from each
283 lineage by remdesivir. **f**, Mutations in 3CL^{pro} found in the indicated passages from each lineage.
284 Dots indicate wild-type at that residue. Mutations are shaded according to frequency. **g**, Residues
285 mutated in passaging in Vero E6 cells overlaid onto the 3CL^{pro} structure with nirmatrelvir bound.
286 The C α of each residue that was mutated is denoted with a red sphere. The 3CL^{pro}-nirmatrelvir
287 complex was downloaded from PDB under accession code 7VH8. Error bars denote mean \pm s.e.m
288 of four technical replicates in **a-e**.

289

290 **Fig. 2. Identification of nirmatrelvir resistance at scale in Huh7-ACE2 cells.** **a**, Passaging
291 scheme. 480 wells were infected with SARS-CoV-2-mNeonGreen and passaged to fresh Huh7-
292 ACE2 cells every 3-4 days, with the concentration of drug doubled every two passages. **b**,
293 Validation of nirmatrelvir resistance of three wells from passage 16. These viral populations had
294 the following mutations: 3A8 (T21I, T304I), 1E11 (T21I, N51Y, T304I), 5A2 (L50F, E166V). See
295 **Supplemental Table 1** for exact frequencies. Representative curves from a single experiment from
296 two biologically independent experiments are shown. Error bars denote mean \pm s.e.m of three
297 technical replicates. **c**, Mutations in 3CL^{pro} found in passage 16 from 53 wells. Dots indicate wild-
298 type at that residue. Mutations are shaded according to frequency. **d**, Residues mutated in
299 passaging in Huh7-ACE2 cells overlaid onto the 3CL^{pro} structure with nirmatrelvir bound. All 23
300 mutated residues across all the resistant populations are indicated with any individual isolate
301 having between 1-6 mutations. The C α of each residue that was mutated is denoted with a red
302 sphere for mutations observed more than 10 times, and denoted with an orange sphere for
303 mutations observed fewer than 10 times. The 3CL^{pro}-nirmatrelvir complex was downloaded from
304 PDB under accession code 7VH8.

305

306 **Fig. 3. Pathways for SARS-CoV-2 resistance to nirmatrelvir. a**, Phylogenetic tree of sequences
307 from passaging in Huh7-ACE2 cells. Only sequences with mutations are shown. Sequences are
308 denoted as passage number, followed by the well number. Mutations that arose along particular
309 branches are annotated in red, “-” denotes when a mutation appears to be lost from a particular
310 branch. **b**, Observed pathways for nirmatrelvir resistance in Huh7-ACE2 cells. The most
311 commonly observed mutations in passage 16 were used to build these pathways (see **Methods and**
312 **Supplemental Table 2** for additional details). Nodes are colored from dark to light, with founder
313 mutations colored darker. Percentages indicate the frequency by which the child nodes derive from
314 the immediate parental node. Descendent arrows that do not sum to 100% indicate that a proportion
315 did not advance beyond the indicated mutations in the experiment. **c**, Growth assay with
316 recombinant live SARS-CoV-2 carrying single and combination 3CL^{pro} mutations. Huh7-ACE2
317 cells were infected with 0.01 MOI of virus and luminescence was quantified at the indicated time
318 points. S144A, E166V, and T21I + S144A are statistically significant from WT at 48 h (two-way
319 ANOVA with Geisser-Greenhouse correction followed by Dunnett’s multiple comparisons test;
320 P=0.0039, P=0.0006, P=0.0006, respectively). Representative curves from a single experiment
321 from two biologically independent experiments are shown. Error bars denote mean ± s.e.m of three
322 technical replicates.

323
324 **Fig. 4. Validation of identified mutations in isogenic recombinant SARS-CoV-2. a**, Individual
325 inhibition curves of recombinant live SARS-CoV-2 carrying single and combination 3CL^{pro}
326 mutations by nirmatrelvir. Representative curves from a single experiment from three biologically
327 independent experiments are shown. Error bars denote mean ± s.e.m of three technical replicates.
328 **b**, Inhibition of recombinant live SARS-CoV-2 carrying single and combination 3CL^{pro} mutations
329 by nirmatrelvir, ensitrelvir, and remdesivir. Values shown are fold change of mean values in IC₅₀
330 relative to inhibition of wild-type from three biologically independent experiments.

331
332 **Extended Data Fig. 1. Growth assays with SARS-CoV-2 passaged in Vero E6 cells. a-d**,
333 Growth was quantified for lineage A (**a**), lineage B (**b**), lineage C (**c**), and unpassaged SARS-CoV-
334 2 (**d**, denoted as WT-P0) in comparison to SARS-CoV-2 passaged without nirmatrelvir for 30
335 passages (denoted as WT-P30). Vero E6 cells were infected with 200 TCID₅₀ of the indicated

336 viruses and viral RNA was quantified at the indicated time points. **e**, The slope during the
337 exponential phase (between 11 and 24 hours post-infection) of growth for the indicated viruses.

338

339 **Extended Data Fig. 2. Mutations in the 11 3CL^{pro} cut sites found in passage 16 from the 53**
340 **wells passaged in Huh7-ACE2 cells.** Dots indicate wild-type at that cut site. Note that nsp4/5
341 M(P6')I = M6I, nsp5/6 S(P6)P = S301P, and nsp5/6 T(P3)I = T304I.

342

343 **Extended Data Fig. 3. Mutations studied as isogenic recombinant SARS-CoV-2 overlaid onto**
344 **the 3CL protease structure.** The C α of each residue that was mutated is denoted with a red sphere.
345 The 3CL^{pro}-nirmatrelvir complex was downloaded from PDB under accession code 7VH8.

346

347 **Extended Data Fig. 4. Raw IC₅₀ values for recombinant live SARS-CoV-2 carrying single**
348 **and combination 3CL^{pro} mutations by nirmatrelvir, ensitrelvir, and remdesivir.** Mean \pm SD
349 of three biologically independent experiments are shown.

350

351 **Extended Data Fig. 5. Individual inhibition curves of recombinant live SARS-CoV-2**
352 **carrying single and combination 3CL^{pro} mutations by ensitrelvir and remdesivir.**
353 Representative curves from a single experiment from three biologically independent experiments
354 are shown. Error bars denote mean \pm s.e.m of three technical replicates.

355

356 **Extended Data Fig. 6. Inhibition of passage 30 of SARS-CoV-2 passaged in Vero E6 cells by**
357 **nirmatrelvir, ensitrelvir, and remdesivir. a**, Raw IC₅₀ values. **b**, Fold change relative to
358 inhibition of wild-type.

359

360 **Extended Data Fig. 7. Structural analyses of 3CL^{pro} mutations. a**, Overlay of nirmatrelvir and
361 ensitrelvir binding to 3CL^{pro}. **b**, Several of the residues involved in direct interaction with
362 nirmatrelvir. **c**, Several of the residues involved in formation of the S1 subsite. **d**, Interaction of
363 L167 with nirmatrelvir. In **a-d**, nirmatrelvir is shown in yellow, ensitrelvir is shown in lime green,
364 the 3CL^{pro}-nirmatrelvir complex is shown in marine, and the 3CL^{pro}-ensitrelvir complex is shown
365 in gray. Protomer A is shown in marine and protomer B is shown in green. Hydrogen bonds are

366 indicated as black dashes. The 3CL^{pro}-nirmatrelvir complex and 3CL^{pro}-ensitrelvir complex were
367 downloaded from PDB under accession codes 7VH8 and 7VU6, respectively.

368

369 **Extended Data Fig. 8. Frequencies of identified 3CL^{pro} mutations in GISAID.** **a,** All
370 occurrences of the indicated mutations were tabulated from GISAID. **b,** All occurrences of the
371 indicated mutations were tabulated from GISAID in the three months prior to EUA (9/22/2021 to
372 12/22/2021) or after EUA (3/26/2022 to 6/26/2022).

373

374

ACCELERATED ARTICLE PREVIEW

375 **References**

376

377 1 Hammond, J. *et al.* Oral Nirmatrelvir for High-Risk, Nonhospitalized Adults with Covid-
378 19. *N Engl J Med* **386**, 1397-1408, doi:10.1056/NEJMoa2118542 (2022).

379 2 Owen, D. R. *et al.* An oral SARS-CoV-2 M(pro) inhibitor clinical candidate for the
380 treatment of COVID-19. *Science* **374**, 1586-1593, doi:10.1126/science.abl4784 (2021).

381 3 Altarawneh, H. N. *et al.* Effects of Previous Infection and Vaccination on Symptomatic
382 Omicron Infections. *N Engl J Med*, doi:10.1056/NEJMoa2203965 (2022).

383 4 Iketani, S. *et al.* Antibody evasion properties of SARS-CoV-2 Omicron sublineages.
384 *Nature* **604**, 553-556, doi:10.1038/s41586-022-04594-4 (2022).

385 5 Liu, L. *et al.* Striking antibody evasion manifested by the Omicron variant of SARS-
386 CoV-2. *Nature* **602**, 676-681, doi:10.1038/s41586-021-04388-0 (2022).

387 6 Planas, D. *et al.* Reduced sensitivity of SARS-CoV-2 variant Delta to antibody
388 neutralization. *Nature* **596**, 276-280, doi:10.1038/s41586-021-03777-9 (2021).

389 7 Wang, P. *et al.* Antibody resistance of SARS-CoV-2 variants B.1.351 and B.1.1.7.
390 *Nature* **593**, 130-135, doi:10.1038/s41586-021-03398-2 (2021).

391 8 Wang, Q. *et al.* Antibody evasion by SARS-CoV-2 Omicron subvariants BA.2.12.1,
392 BA.4, and BA.5. *bioRxiv*, doi:https://doi.org/10.1101/2022.05.26.493517 (2022).

393 9 Gandhi, S. *et al.* De novo emergence of a remdesivir resistance mutation during treatment
394 of persistent SARS-CoV-2 infection in an immunocompromised patient: a case report.
395 *Nat Commun* **13**, 1547, doi:10.1038/s41467-022-29104-y (2022).

396 10 Baden, L. R. *et al.* Efficacy and Safety of the mRNA-1273 SARS-CoV-2 Vaccine. *N*
397 *Engl J Med* **384**, 403-416, doi:10.1056/NEJMoa2035389 (2021).

398 11 Chen, P. *et al.* SARS-CoV-2 Neutralizing Antibody LY-CoV555 in Outpatients with
399 Covid-19. *N Engl J Med* **384**, 229-237, doi:10.1056/NEJMoa2029849 (2021).

400 12 Dougan, M. *et al.* Bebtelovimab, alone or together with bamlanivimab and etesevimab, as
401 a broadly neutralizing monoclonal antibody treatment for mild to moderate, ambulatory
402 COVID-19. *medRxiv*, doi:https://doi.org/10.1101/2022.03.10.22272100 (2022).

403 13 Gupta, A. *et al.* Early Treatment for Covid-19 with SARS-CoV-2 Neutralizing Antibody
404 Sotrovimab. *N Engl J Med* **385**, 1941-1950, doi:10.1056/NEJMoa2107934 (2021).

405 14 Polack, F. P. *et al.* Safety and Efficacy of the BNT162b2 mRNA Covid-19 Vaccine. *N*
406 *Engl J Med* **383**, 2603-2615, doi:10.1056/NEJMoa2034577 (2020).

407 15 Sadoff, J. *et al.* Safety and Efficacy of Single-Dose Ad26.COV2.S Vaccine against
408 Covid-19. *N Engl J Med* **384**, 2187-2201, doi:10.1056/NEJMoa2101544 (2021).

409 16 Weinreich, D. M. *et al.* REGN-COV2, a Neutralizing Antibody Cocktail, in Outpatients
410 with Covid-19. *N Engl J Med* **384**, 238-251, doi:10.1056/NEJMoa2035002 (2021).

- 411 17 Beigel, J. H. *et al.* Remdesivir for the Treatment of Covid-19 - Final Report. *N Engl J*
412 *Med* **383**, 1813-1826, doi:10.1056/NEJMoa2007764 (2020).
- 413 18 Gottlieb, R. L. *et al.* Early Remdesivir to Prevent Progression to Severe Covid-19 in
414 Outpatients. *N Engl J Med* **386**, 305-315, doi:10.1056/NEJMoa2116846 (2022).
- 415 19 Fischer, W. A., 2nd *et al.* A phase 2a clinical trial of molnupiravir in patients with
416 COVID-19 shows accelerated SARS-CoV-2 RNA clearance and elimination of infectious
417 virus. *Sci Transl Med* **14**, eab17430, doi:10.1126/scitranslmed.ab17430 (2022).
- 418 20 Jayk Bernal, A. *et al.* Molnupiravir for Oral Treatment of Covid-19 in Nonhospitalized
419 Patients. *N Engl J Med* **386**, 509-520, doi:10.1056/NEJMoa2116044 (2022).
- 420 21 Painter, W. P. *et al.* Human Safety, Tolerability, and Pharmacokinetics of Molnupiravir, a
421 Novel Broad-Spectrum Oral Antiviral Agent with Activity Against SARS-CoV-2.
422 *Antimicrob Agents Chemother*, doi:10.1128/AAC.02428-20 (2021).
- 423 22 Chan, A. P., Choi, Y. & Schork, N. J. Conserved Genomic Terminals of SARS-CoV-2 as
424 Coevolving Functional Elements and Potential Therapeutic Targets. *mSphere* **5**,
425 doi:10.1128/mSphere.00754-20 (2020).
- 426 23 V'Kovski, P., Kratzel, A., Steiner, S., Stalder, H. & Thiel, V. Coronavirus biology and
427 replication: implications for SARS-CoV-2. *Nat Rev Microbiol* **19**, 155-170,
428 doi:10.1038/s41579-020-00468-6 (2021).
- 429 24 Stevens, L. J. *et al.* Mutations in the SARS-CoV-2 RNA dependent RNA polymerase
430 confer resistance to remdesivir by distinct mechanisms. *Sci Transl Med*, eabo0718,
431 doi:10.1126/scitranslmed.abo0718 (2022).
- 432 25 Szemiel, A. M. *et al.* In vitro selection of Remdesivir resistance suggests evolutionary
433 predictability of SARS-CoV-2. *PLoS Pathog* **17**, e1009929,
434 doi:10.1371/journal.ppat.1009929 (2021).
- 435 26 Hoffman, R. L. *et al.* Discovery of Ketone-Based Covalent Inhibitors of Coronavirus
436 3CL Proteases for the Potential Therapeutic Treatment of COVID-19. *J Med Chem* **63**,
437 12725-12747, doi:10.1021/acs.jmedchem.0c01063 (2020).
- 438 27 Xie, X. *et al.* An Infectious cDNA Clone of SARS-CoV-2. *Cell Host Microbe* **27**, 841-
439 848 e843, doi:10.1016/j.chom.2020.04.004 (2020).
- 440 28 Unoh, Y. *et al.* Discovery of S-217622, a Noncovalent Oral SARS-CoV-2 3CL Protease
441 Inhibitor Clinical Candidate for Treating COVID-19. *J Med Chem* **65**, 6499-6512,
442 doi:10.1021/acs.jmedchem.2c00117 (2022).
- 443 29 Mukae, H. *et al.* A Randomized Phase 2/3 Study of Ensitrelvir, a Novel Oral SARS-CoV-
444 2 3C-like Protease Inhibitor, in Japanese Patients With Mild-to-Moderate COVID-19 or
445 Asymptomatic SARS-CoV-2 Infection: Results of the Phase 2a Part. *medRxiv*,
446 doi:https://doi.org/10.1101/2022.05.17.22275027 (2022).
- 447 30 Ferreira, J. C., Fadl, S. & Rabeh, W. M. Key dimer interface residues impact the catalytic
448 activity of 3CLpro, the main protease of SARS-CoV-2. *J Biol Chem* **298**, 102023,
449 doi:10.1016/j.jbc.2022.102023 (2022).

- 450 31 Shu, Y. & McCauley, J. GISAID: Global initiative on sharing all influenza data - from
451 vision to reality. *Euro Surveill* **22**, doi:10.2807/1560-7917.ES.2017.22.13.30494 (2017).
- 452 32 (ASPR), H. O. o. t. A. S. f. P. a. R. *COVID-19 Therapeutics Thresholds, Orders, and*
453 *Replenishment by Jurisdiction*, <[https://aspr.hhs.gov/COVID-](https://aspr.hhs.gov/COVID-19/Therapeutics/orders/Pages/default.aspx)
454 [19/Therapeutics/orders/Pages/default.aspx](https://aspr.hhs.gov/COVID-19/Therapeutics/orders/Pages/default.aspx)> (2022).
- 455 33 Iketani, S. *et al.* The Functional Landscape of SARS-CoV-2 3CL Protease. *bioRxiv*,
456 doi:<https://doi.org/10.1101/2022.06.23.497404> (2022).
- 457 34 Jochmans, D. *et al.* The substitutions L50F, E166A and L167F in SARS-CoV-2 3CLpro
458 are selected by a protease inhibitor in vitro and confer resistance to nirmatrelvir. *bioRxiv*,
459 doi:<https://doi.org/10.1101/2022.06.07.495116> (2022).
- 460 35 Zhou, Y. *et al.* Nirmatrelvir Resistant SARS-CoV-2 Variants with High Fitness in Vitro.
461 *bioRxiv*, doi:<https://doi.org/10.1101/2022.06.06.494921> (2022).
- 462 36 Xue, X. *et al.* Structures of two coronavirus main proteases: implications for substrate
463 binding and antiviral drug design. *J Virol* **82**, 2515-2527, doi:10.1128/JVI.02114-07
464 (2008).
- 465 37 Yang, S. *et al.* Synthesis, crystal structure, structure-activity relationships, and antiviral
466 activity of a potent SARS coronavirus 3CL protease inhibitor. *J Med Chem* **49**, 4971-
467 4980, doi:10.1021/jm0603926 (2006).
- 468 38 Zhao, Y. *et al.* Crystal structure of SARS-CoV-2 main protease in complex with protease
469 inhibitor PF-07321332. *Protein Cell* **13**, 689-693, doi:10.1007/s13238-021-00883-2
470 (2022).
- 471 39 Padhi, A. K. & Tripathi, T. Hotspot residues and resistance mutations in the nirmatrelvir-
472 binding site of SARS-CoV-2 main protease: Design, identification, and correlation with
473 globally circulating viral genomes. *Biochem Biophys Res Commun* **629**, 54-60,
474 doi:10.1016/j.bbrc.2022.09.010 (2022).
- 475 40 Shaqra, A. M. *et al.* Defining the substrate envelope of SARS-CoV-2 main protease to
476 predict and avoid drug resistance. *Nat Commun* **13**, 3556, doi:10.1038/s41467-022-
477 31210-w (2022).
- 478 41 Yang, K. S., Leeuwon, S. Z., Xu, S. & Liu, W. R. Evolutionary and Structural Insights
479 about Potential SARS-CoV-2 Evasion of Nirmatrelvir. *J Med Chem* **65**, 8686-8698,
480 doi:10.1021/acs.jmedchem.2c00404 (2022).
- 481 42 Sacco, M. D. *et al.* The P132H mutation in the main protease of Omicron SARS-CoV-2
482 decreases thermal stability without compromising catalysis or small-molecule drug
483 inhibition. *Cell Res* **32**, 498-500, doi:10.1038/s41422-022-00640-y (2022).

484
485

486 **Methods**

487

488 **Biosafety**

489 All SARS-CoV-2 passaging, infection, and recombinant virus production was conducted in BSL-
490 3 laboratories at Columbia University Irving Medical Center under procedures and guidelines
491 approved by the Columbia University Institutional Biosafety Committee (IBC).

492

493 **Compounds**

494 Nirmatrelvir was purchased from Aobius, ensitrelvir was purchased from Glix Laboratories, and
495 remdesivir was purchased from Selleckchem.

496

497 **Cells**

498 Vero E6 cells were obtained from ATCC (Catalog #CRL-1586), HEK293T cells were obtained
499 from ATCC (Catalog #CRL-3216), and Vero E6-TMPRSS2-T2A-ACE2 cells were obtained from
500 BEI Resources (Catalog #NR-54970). Huh7-ACE2 cells were generated previously^{33,43}. Cell
501 morphology was visually confirmed prior to use and all cell lines tested mycoplasma negative. All
502 cells were maintained at 37 °C under 5% CO₂.

503

504 **In vitro selection for SARS-CoV-2 resistance to nirmatrelvir in Vero E6 cells**

505 To select for the development of drug resistance against nirmatrelvir, WA1 (SARS-CoV-2, USA-
506 WA1/2020 strain) was cultured in the presence of increasing concentrations of nirmatrelvir and
507 passaged 30 times. Virus isolates recovered from the culture at various passages were then
508 characterized for their resistance to nirmatrelvir and their replication capacity.

509

510 To initiate the passaging, Vero E6 cells were seeded in a 24 well-plate at a density of 1×10^5 cells
511 per well in complete media (DMEM + 10% FCS + penicillin/streptomycin), and then the drug and
512 virus were added the following day. The drug was prepared in a three-fold dilution series based on
513 the original IC₅₀ of the drug. The virus was added at 5,000 TCID₅₀ per well. Three days post-
514 infection, each well was scored for cytopathic effects (CPE) in a range of 0 to 4+ based on
515 comparison to control wells as previously described⁴⁴, and 100 μL of the supernatant from the well
516 with a CPE score equal to or greater than 2+ was passaged to each well in the next culture plate.

517 The passage culture was set up in triplicate (lineages A, B, and C) and the passaging was performed
518 independently, i.e., viruses in lineage A were kept within the lineage A series of wells at every
519 passage. Along with the cultures passaged with nirmatrelvir, WA1 was passaged without
520 nirmatrelvir in two independent wells to serve as a passage control.

521
522 IC₅₀s for each lineage in the passaging were determined based on the CPE scores at day 3 of each
523 passage. IC₅₀ values were derived by using DeltaGraph (Red Rock Software).

524
525 **Sequencing of SARS-CoV-2 passaged in Vero E6 cells**

526 For the SARS-CoV-2 passaged in Vero E6 cells, passages were sequenced by Sanger sequencing
527 or by Nanopore sequencing. For Sanger sequencing, viral RNA was isolated from the culture
528 supernatant with QIAamp® Viral RNA Mini Kit (Qiagen), reverse transcribed to cDNA with
529 Superscript IV™ Reverse Transcriptase (Thermo Fisher) and the priming primer, nsp5.R1, and
530 subjected to nested PCR with Platinum™ SuperFi II (Thermo Fisher) to obtain the full length nsp5
531 gene. The primers for the first PCR are nsp5.F1: 5'-GTAGTGATGTGCTATTACCTCTTACGC-
532 3' and nsp5.R1: 5'- GCAAAAGCAGACATAGCAATAATACC-3'. The primers for the second
533 PCR are nsp5.F2: 5'-CTTCAGTAACTCAGGTTCTGATGTTCT-3' and nsp5.R2: 5'-
534 ACCATTGAGTACTCTGGACTAAAATAAAA-3'. Both PCRs were run with the same condition
535 of 98 °C for 30 s, 25 cycles of 98 °C for 15 s, 60 °C for 10 s, and 72 °C for 1 min, followed by
536 72 °C for 5 min. The PCR products were purified and sequenced (Genewiz). Mixtures of viruses
537 were determined by inspecting sequencing chromatograms. The sequences were analyzed using
538 Lasergene software (DNASTAR).

539
540 For Nanopore sequencing, viral RNA was isolated from the culture supernatant with QIAamp®
541 Viral RNA Mini Kit (Qiagen), and then the Midnight RT PCR Expansion kit and Rapid Barcoding
542 kits (Oxford Nanopore) were used to amplify and barcode overlapping 1,200 bp amplicons tiled
543 across the viral genome^{45,46}. An Oxford Nanopore GridION with R9.4.1 flow cells was used for
544 sequencing. Basecalling was performed in MinKNOW v22.05.1. Consensus sequence generation
545 was performed using the ONT Epi2Me ARTIC Nextflow pipeline v0.3.16
546 (<https://github.com/epi2me-labs/wf-artic>). Pangolin 4.0.6 with UShER v1.6 was used for

547 parsimony-based lineage assignment. Sequences have been deposited to GenBank (ON924329-
548 ON924335, ON930401-ON930431) (**Supplemental Table 3**).

549

550 **Inhibition assay with SARS-CoV-2 passaged in Vero E6 cells**

551 To characterize the inhibition of passaged viruses, each of the viruses were first propagated in
552 Vero E6 cells in the absence of drug and titrated by the Reed-Muench method⁴⁷. Vero E6 cells
553 were then seeded in 96 well-plates at a density of 1.5×10^4 cells per well in complete media. The
554 following day, the virus was inoculated at a dose of 500 TCID₅₀ per well, and a two-fold dilution
555 series of inhibitor was added in quadruplicate. Three days post-infection, the level of CPE was
556 scored and the IC₅₀ was derived by fitting a nonlinear regression curve to the data in GraphPad
557 Prism version 9.4 (Dotmatics).

558

559 **Growth assay with SARS-CoV-2 passaged in Vero E6 cells**

560 The fitness of passaged viruses was characterized by a viral growth assay. Vero E6 cells were
561 seeded in 96 well-plates at a density of 1.5×10^4 cells per well in complete media. The following
562 day, the virus was inoculated at a dose of 200 TCID₅₀ per well in quadruplicate. At 6 h post-
563 infection, free virions in the culture were removed by changing of the media twice. At 11, 24, 35,
564 and 49 h post-infection, 50 μ L of the culture supernatant from each well was collected and
565 replenished with an equivalent volume of fresh media. Viral RNA from each time point was
566 purified by using PureLink™ Pro 96 Viral RNA/DNA Purification Kit (Thermo Fisher) and then
567 the viral copy number in each sample was estimated by qRT-PCR using TaqPath™ 1-Step RT-
568 qPCR Master Mix (Thermo Fisher) and 2019-nCov CDC EUA Kit (Integrated DNA
569 Technologies) with 7500 Fast Dx Real-Time PCR Instrument (Applied Biosystems).

570

571 **In vitro selection for SARS-CoV-2 resistance to nirmatrelvir in Huh7-ACE2 cells**

572 To conduct selection at scale to observe as many resistance pathways as possible, SARS-CoV-2
573 infection was conducted in five 96 well-plates, thereby allowing for 480 independent selection
574 lineages. We hypothesized that the use of limited number of cells allowed for a “bottleneck effect”
575 to occur, which enabled observation of rarer events that may be outcompeted from a larger
576 population.

577

578 To initiate the passaging, 3×10^4 Huh7-ACE2 cells per well were seeded in complete media in
579 five 96 well-plates. The following day, all wells were infected with 0.05 MOI of SARS-CoV-2-
580 mNeonGreen (a fluorescent reporter variant of USA-WA1/2020, gift of Pei-Yong Shi)²⁷ without
581 drug to generate passage 0 (P0). For each successive passage, cells were seeded the day prior to
582 infection, and then the drug and virus were added, three to four days post-infection of the previous
583 passage. The drug was initially added at 25 nM and then doubled every other successive passage.
584 Viruses were transferred between passages by overlaying 50 μ L of the supernatant from the
585 previous passage. After 16 passages, all 54 wells positive for mNeonGreen signal were sequenced,
586 of which 53 lineages could be determined.

587

588 **Inhibition assay with SARS-CoV-2 passaged in Huh7-ACE2 cells**

589 To characterize the inhibition of passaged viruses, each of the viruses were first propagated in
590 Huh7-ACE2 cells in the absence of drug and titrated by the Reed-Muench method⁴⁷. Huh7-ACE2
591 cells were then seeded in 96 well-plates at a density of 2×10^4 cells per well in complete media.
592 The following day, the virus was inoculated at a dose of 0.05 MOI per well, and a five-fold dilution
593 series of inhibitor was added in triplicate. At 24 h post-infection, the supernatant was aspirated and
594 cells were fixed with 4% PFA in PBS and stained with DAPI. Cells were then imaged for DAPI
595 and GFP using IN Cell 2000 (GE) and analyzed with CellProfiler version 4.0.7⁴⁸. The IC₅₀ was
596 then derived by fitting a nonlinear regression curve to the data in GraphPad Prism version 9.4
597 (Dotmatics).

598

599 **Sequencing of SARS-CoV-2 passaged in Huh7-ACE2 cells**

600 For the SARS-CoV-2 passaged in Huh7-ACE2 cells, passages were sequenced by Illumina next-
601 generation sequencing. Viral RNA was first extracted using PureLink™ Pro 96 Viral RNA/DNA
602 Purification Kit (Thermo Fisher). Reverse transcription was carried out using Maxima H Minus
603 First Strand cDNA Synthesis Kit (Thermo Fisher) with random hexamers according to the
604 manufacturer's instructions. Briefly, 13.75 μ L of viral RNA was mixed with 0.25 μ L random
605 hexamers (50 ng/ μ L) and 1 μ L dNTPs (10 mM), and incubated at 65 °C for 5 min followed by
606 4 °C for 1 min. Then, a mixture containing 4 μ L 5x RT buffer, 0.25 μ L enzyme mix (containing
607 Maxima H Minus RT and RNase inhibitor), and 0.75 μ L H₂O was added to each sample and the
608 reactions were incubated at 25 °C for 10 min, 55 °C for 30 min, and 85 °C for 5 min.

609

610 Sequencing libraries were prepared by amplifying either nine fragments tiled across the 3CL^{pro}
611 open reading frame and adjacent nsp4/5 and nsp5/6 cut sites, or nine fragments containing each of
612 the remaining 3CL^{pro} cut sites (see **Supplemental Table 4** for primer sequences). Primers
613 amplifying non-adjacent fragments of the 3CL^{pro} were pooled together and reactions were carried
614 out in technical duplicate, for a total of four first-round PCRs per sample. Each first-round PCR
615 contained the following components: 1 μ L cDNA, 0.25 μ L 100 μ M pooled primers, 0.4 μ L 10
616 mM dNTPs, 2 μ L 10x Taq buffer, 0.1 μ L Taq DNA polymerase (Enzymatics), and 16.25 μ L H₂O.
617 Cycling conditions were as follows: (1) 94 °C, 3 min, (2) 94 °C, 30 s, (3) 54 °C, 20 s, (4) 72 °C,
618 30 s, (5) Return to step #2 for 34 additional cycles, (6) 72 °C, 3 min, (7) Hold at 4 °C.

619

620 Products from the four first-round PCRs for each sample were pooled and gel purified, and a
621 second-round indexing PCR was carried out for each sample with the following reagents: 1 μ L
622 template DNA, 0.25 μ L each 100 μ M indexing primer, 0.4 μ L 10 mM dNTPs, 2 μ L 10x Taq buffer,
623 0.1 μ L Taq DNA polymerase, and 16.25 μ L H₂O. The cycling conditions were as follows: (1)
624 94 °C, 3 min, (2) 94 °C, 30 s, (3) 54 °C, 20 s, (4) 72 °C, 30 s, (5) Return to step #2 for 6 additional
625 cycles, (6) 72 °C, 3 min, (7) Hold at 4 °C.

626

627 Second round PCR products were pooled, gel purified, and sequenced on an Illumina NextSeq
628 system with 150 bp single-end reads. For select samples, sequences were confirmed using
629 nanopore sequencing (Plasmidsaurus). For samples P16-2D9, P12-1A4, and 4-3A1, the original
630 Illumina sequencing results were replaced with the Nanopore sequencing results.

631

632 For each sample, mutations and their frequencies were identified using the V-pipe computational
633 pipeline (version 2.99.2)⁴⁹, with Wuhan-Hu-1 (GenBank accession no. MN908947) set as the
634 reference sequence. Frequency thresholds for reporting mutations were set at 5% and 10% for
635 Illumina and nanopore sequencing, respectively. See **Supplemental Table 1** for absolute
636 frequencies of mutations within each sample. Raw sequencing data have been deposited to NCBI
637 Short Read Archive under BioProject Accession ID PRJNA852265 (see **Supplemental Table 5**
638 for SRA Accession IDs for each sample). These sequences were clustered for **Fig. 2c** using
639 seaborn.clustermap under default settings, which utilizes the UPGMA algorithm through SciPy^{50,51}.

640 The phylogenetic analysis shown in **Extended Data Fig. 3** was produced in Geneious Prime
641 v2022.1 with PHYML extension, using the GTR substitution model with the optimization
642 conditions of topology/length/rate.

643

644 **Pathway analysis for SARS-CoV-2 passaged in Huh7-ACE2 cells**

645 **Fig. 3a** was constructed from lineages containing only the mutations that were found most
646 commonly in passage 16: T21I, T304I, A173V, E166V, P252L, S144A, and L50F. These lineages
647 were determined based on the frequencies of the corresponding mutations in a given well at each
648 passage. Pairs of mutants whose frequencies summed to greater than 100% were assumed to co-
649 occur on the same allele. The same logic was extended to identify triple and quadruple mutants,
650 such that if each pairwise sum of frequencies within a group of mutations was greater than 100%,
651 all mutations within that group were assumed to occur together. The order in which mutations in
652 a given lineage arose was imputed either from stepwise appearance over time (e.g., passage 4 has
653 mutation 1 and passage 8 has mutation 1 and mutation 2 at a total combined frequency >100%)
654 with increasing frequencies, or, in cases where 2 mutations arose between sequenced passages and
655 were deemed to co-occur in a single virus, by their relative frequencies (e.g., if passage 4 has no
656 mutations and passage 8 has mutation 1 at 99% frequency and mutation 2 at 30% frequency,
657 mutation 1 was assumed to have arisen first). See **Supplemental Table 2** for the datapoints used
658 in this analysis.

659

660 **Recombinant SARS-CoV-2 production**

661 A reverse genetics system based on the pBeloBAC11 bacterial artificial chromosome (BAC)
662 containing the SARS-CoV-2 genome with a NanoLuc luciferase reporter replacing ORF7a⁵² (gift
663 of Luis-Martinez Sobrido) was used to produce recombinant SARS-CoV-2 harboring 3CL^{pro}
664 mutations. Mutants BACs were produced as previously described³³; see **Supplemental Table 6**
665 for a list of mutagenic primers used. These BACs (2 µg each) were then transfected into HEK293T
666 cells in 12 well-plates in triplicate using Lipofectamine™ 3000 Transfection Reagent (Thermo
667 Fisher) according to the manufacturer's instructions. Two days post-transfection, cells were pooled
668 and overlaid onto Vero E6-TMPRSS2-T2A-ACE2 cells in 25 cm² flasks. After three days, the
669 supernatant was collected from these cells and clarified by centrifugation, then used to infect Vero
670 E6 cells in 75 cm² flasks. Four days post-infection, the supernatant was harvested, clarified by

671 centrifugation, and aliquoted. Viruses were stored at -80 °C prior to use. An aliquot of all
672 recombinant viruses was confirmed by nanopore sequencing for the mutation of interest and for
673 purity prior to use.

674

675 **Inhibition assay with recombinant SARS-CoV-2**

676 Viruses were first titrated to normalize input. To characterize inhibition, Huh7-ACE2 cells were
677 seeded at a density of 2×10^4 cells per well in 96 well-plates. The following day, cells were infected
678 with 0.05 MOI of virus, and treated with inhibitor in a five-fold dilution series. One day post-
679 infection, cells were lysed and luminescence was quantified using the Nano-Glo® Luciferase
680 Assay System (Promega) according to the manufacturer's instructions with a SpectraMax i3x
681 Multi-Mode Microplate Reader (Molecular Devices) using the SoftMax Pro 7.0.2 software
682 (Molecular Devices). IC₅₀s were derived by fitting a nonlinear regression curve to the data in
683 GraphPad Prism version 9.4 (Dotmatics).

684

685 **Growth assay with recombinant SARS-CoV-2**

686 Viruses were first titrated to normalize input. To characterize fitness, Huh7-ACE2 cells were
687 seeded at a density of 2×10^4 cells per well in 96 well-plates. The following day, cells were infected
688 with 0.01 MOI of virus. At 12, 24, 36, and 48 h post-infection, cells were lysed and luminescence
689 was quantified using the Nano-Glo® Luciferase Assay System according to the manufacturer's
690 instructions with a SpectraMax i3x Multi-Mode Microplate Reader using the SoftMax Pro 7.0.2
691 software.

692

693 **Retrieval of clinical mutation frequencies**

694 COVID-19 CG was used to retrieve all clinically observed 3CL^{pro} mutations from GISAID on June
695 26, 2022, either since the start of the COVID-19 pandemic or between March 26-June 26, 2022,
696 and September 22-December 22, 2021^{31,53}.

697 **Acknowledgements**

698 This study was supported by funding from the JPB Foundation, Andrew and Peggy Cherng,
699 Samuel Yin, Carol Ludwig, and David and Roger Wu to D.D.H. A.C. is supported by a Career
700 Awards for Medical Scientists from the Burroughs Wellcome Fund. We thank Pei-Yong Shi for
701 the SARS-CoV-2-mNeonGreen reporter virus and Luis Martinez-Sobrido and Chengjin Ye for
702 the bacterial artificial chromosome system to generate recombinant SARS-CoV-2.

703
704 **Author contributions**

705 S.I., B.C., S.J.H., A.C., and D.D.H. conceived this project and approach to scaled screening for
706 resistant viral variants. S.I. and H.M. conducted the *in vitro* passaging. S.I., H.M., B.C., S.J.H.,
707 M.K.A., A-C.U., and A.C. conducted the sequencing. S.I. and H.M. conducted the fitness and
708 inhibition assays. B.C., S.J.H., and A.C. conducted the pathway analyses. S.I., H.M., B.C.,
709 S.J.H., M.I.L., Y.S., and A.C. generated recombinant SARS-CoV-2. Y.D., Y.G., Z.S., and H.Y.
710 conducted the structural analyses. S.P.G. contributed to discussions of the data and analysis. S.I.,
711 H.M., B.C., S.J.H., Y.D., H.Y., A.C., and D.D.H. wrote the manuscript with input from all
712 authors.

713
714 **Competing interests**

715 S.I., A.C., and D.D.H. are inventors on patent applications related to the development of
716 inhibitors against the SARS-CoV-2 3CL protease. D.D.H. is a co-founder of TaiMed Biologics
717 and RenBio, consultant to WuXi Biologics and Brie Biosciences, and board director for
718 Vicarious Surgical.

719
720 **Materials availability**

721 Materials used in this study will be made available under an appropriate Materials Transfer
722 Agreement.

723
724 **Data availability**

725 All experimental data are provided in the manuscript. The sequences of mutants from passaging
726 in Vero E6 cells have been deposited to GenBank (ON924329-ON924335, ON930401-
727 ON930431). The raw next-generation sequencing data of passaging in Huh7-ACE2 cells are

728 available from the NCBI Short Read Archive under BioProject Accession ID PRJNA852265.
729 The structures of the 3CL^{pro}-nirmatrelvir complex and 3CL^{pro}-ensitrelvir complex were
730 downloaded from PDB under accession codes 7VH8 and 7VU6, respectively. The Wuhan-Hu-1
731 sequence used for alignment was downloaded from GenBank (accession no. MN908947).

732

733 **Code availability**

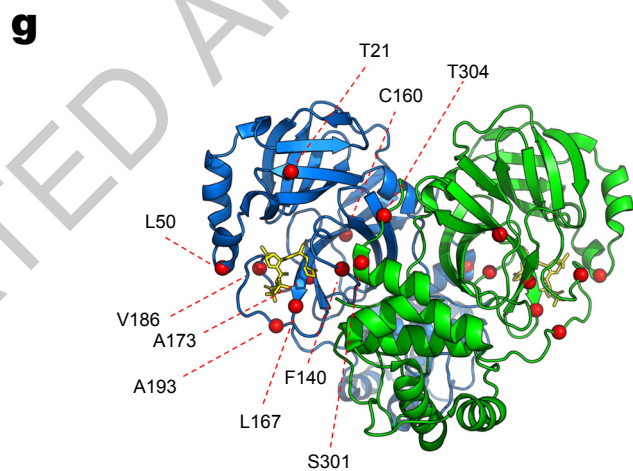
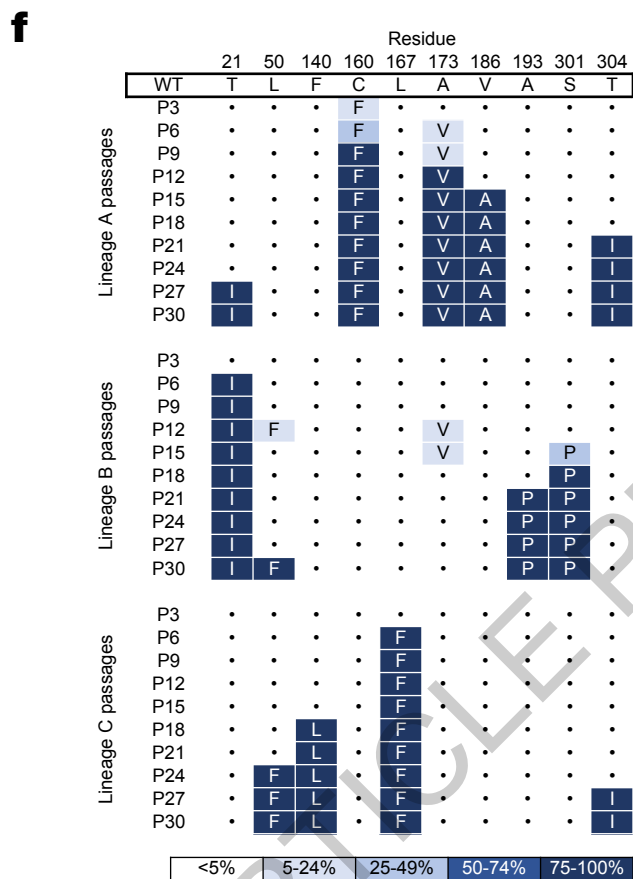
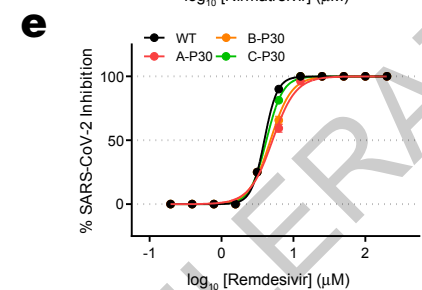
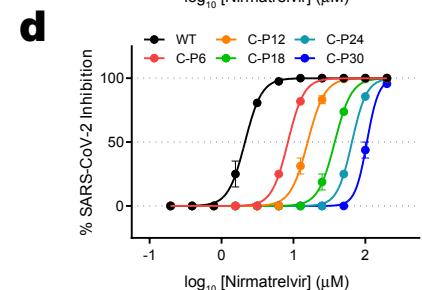
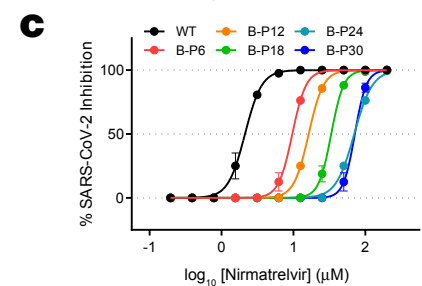
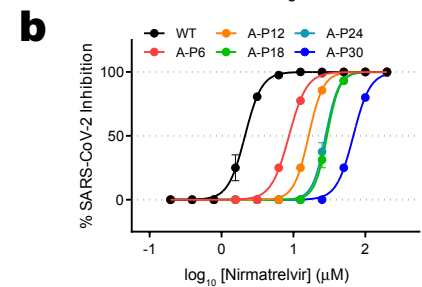
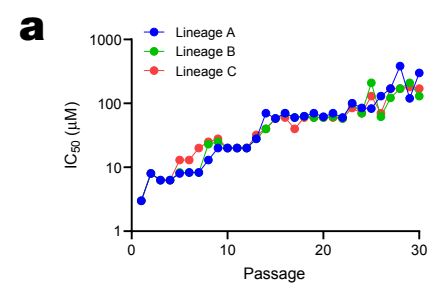
734 Sequencing data processing and visualization was performed using the ONT ARTIC Nextflow
735 pipeline (<https://github.com/epi2me-labs/wf-artic>) and the V-pipe computational pipeline
736 (<https://github.com/cbg-ethz/V-pipe>), and clustering was performed using seaborn
737 (<https://github.com/mwaskom/seaborn>), which utilizes SciPy (<https://github.com/scipy/scipy>), all
738 of which are publicly available software and packages.

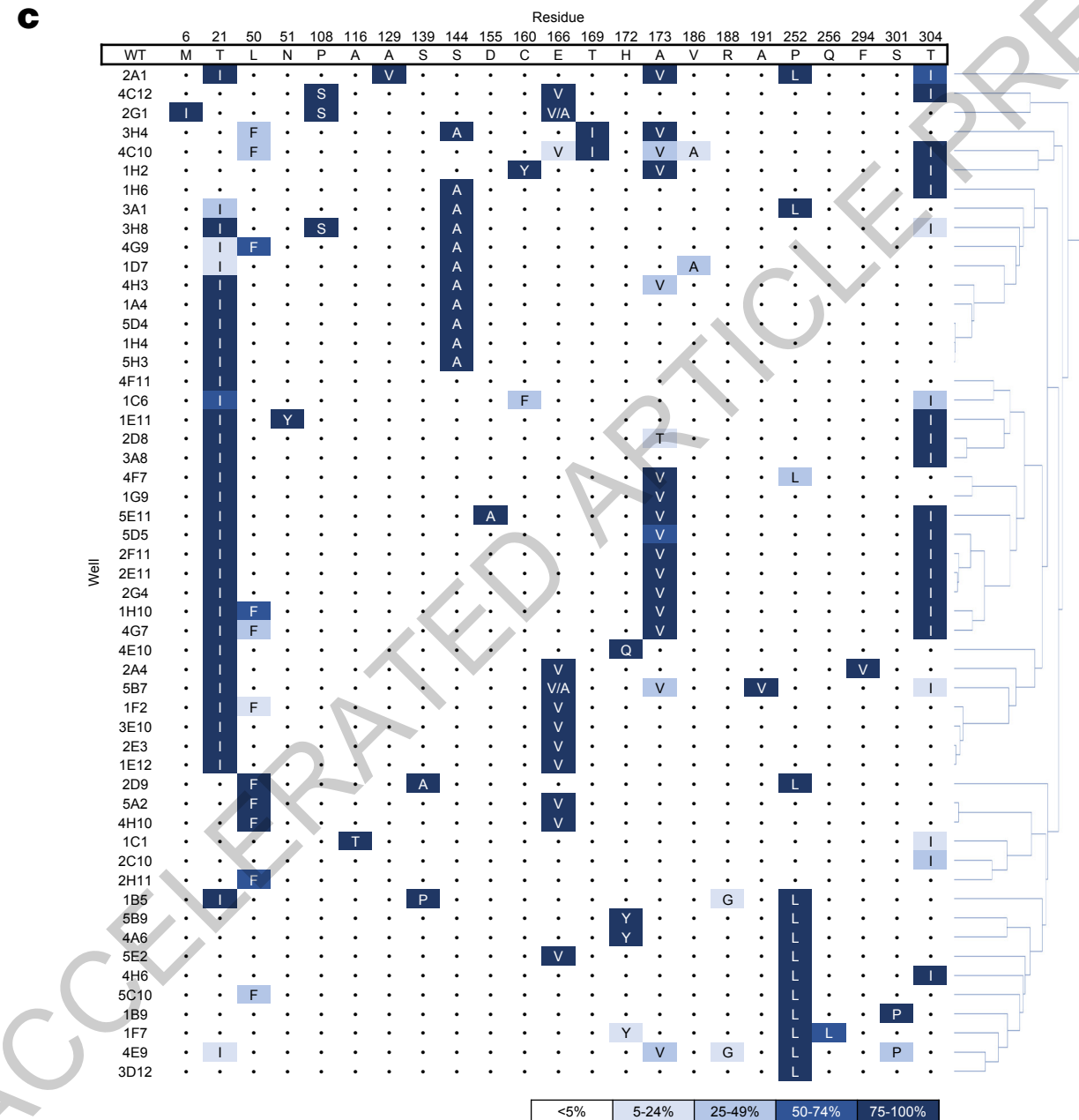
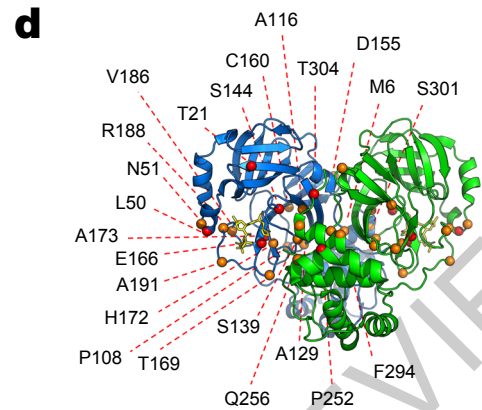
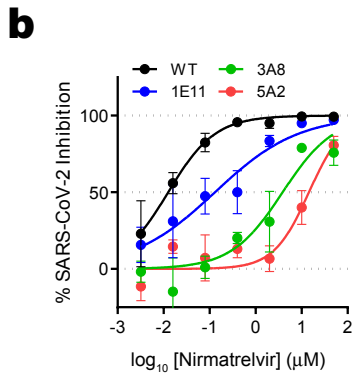
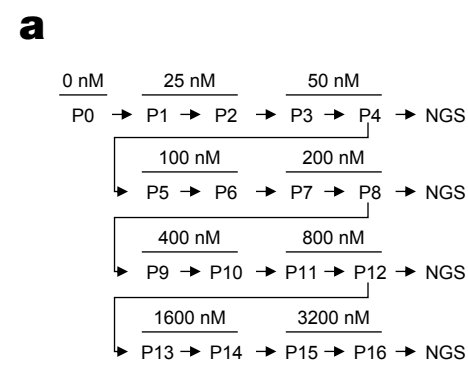
739

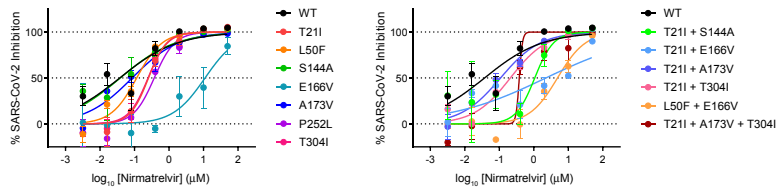
740 **Additional References**

- 741
- 742 43 Liu, H. *et al.* Development of optimized drug-like small molecule inhibitors of the
743 SARS-CoV-2 3CL protease for treatment of COVID-19. *Nat Commun* **13**, 1891,
744 doi:10.1038/s41467-022-29413-2 (2022).
- 745 44 Liu, L. *et al.* Potent neutralizing antibodies against multiple epitopes on SARS-CoV-2
746 spike. *Nature* **584**, 450-456, doi:10.1038/s41586-020-2571-7 (2020).
- 747 45 Freed, N. E., Vlkova, M., Faisal, M. B. & Silander, O. K. Rapid and inexpensive whole-
748 genome sequencing of SARS-CoV-2 using 1200 bp tiled amplicons and Oxford
749 Nanopore Rapid Barcoding. *Biol Methods Protoc* **5**, bpaa014,
750 doi:10.1093/biomethods/bpaa014 (2020).
- 751 46 Annavajhala, M. K. *et al.* Emergence and expansion of SARS-CoV-2 B.1.526 after
752 identification in New York. *Nature* **597**, 703-708, doi:10.1038/s41586-021-03908-2
753 (2021).
- 754 47 Reed, L. J. & Muench, H. A SIMPLE METHOD OF ESTIMATING FIFTY PER CENT
755 ENDPOINTS. *American Journal of Epidemiology* **27**, 493-497,
756 doi:https://doi.org/10.1093/oxfordjournals.aje.a118408 (1938).
- 757 48 Stirling, D. R. *et al.* CellProfiler 4: improvements in speed, utility and usability. *BMC*
758 *Bioinformatics* **22**, 433, doi:10.1186/s12859-021-04344-9 (2021).
- 759 49 Posada-Céspedes, S. *et al.* V-pipe: a computational pipeline for assessing viral genetic
760 diversity from high-throughput data. *Bioinformatics*, doi:10.1093/bioinformatics/btab015
761 (2021).
- 762 50 Virtanen, P. *et al.* SciPy 1.0: fundamental algorithms for scientific computing in Python.
763 *Nat Methods* **17**, 261-272, doi:10.1038/s41592-019-0686-2 (2020).
- 764 51 Waskom, M. L. seaborn: statistical data visualization. *Journal of Open Source Software*
765 **6**, 3021 (2021).
- 766 52 Ye, C. *et al.* Rescue of SARS-CoV-2 from a Single Bacterial Artificial Chromosome.
767 *mBio* **11**, doi:10.1128/mBio.02168-20 (2020).
- 768 53 Chen, A. T., Altschuler, K., Zhan, S. H., Chan, Y. A. & Deverman, B. E. COVID-19 CG
769 enables SARS-CoV-2 mutation and lineage tracking by locations and dates of interest.
770 *Elife* **10**, doi:10.7554/eLife.63409 (2021).

771

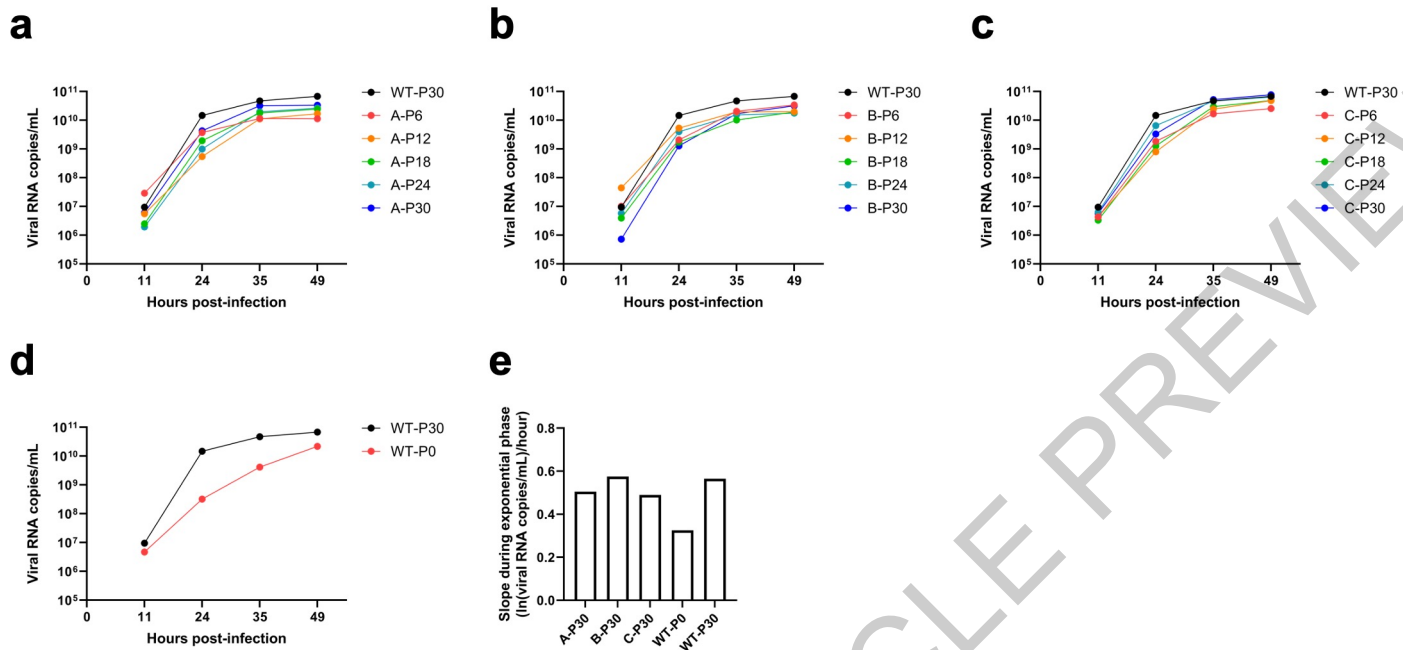




a**b**

Fold change in IC ₅₀ relative to WT	Nirmatrelvir	Ensitrelvir	Remdesivir
T21I	-4.6	-1.7	1.7
L50F	-4.2	-2.8	1.2
S144A	-2.2	-13	2.9
E166V	-100	-23	3.7
A173V	-1.7	-1.7	-2.0
P252L	-5.9	-1.9	1.5
T304I	-5.5	-1.6	1.6
T21I + S144A	-9.4	-18	1.7
T21I + E166V	-83	-3.4	-2.4
T21I + A173V	-3.1	2.0	-2.1
T21I + T304I	-3.3	1.0	2.8
L50F + E166V	-53	-3.7	-1.9
T21I + A173V + T304I	-15	2.1	-2.9

<-5	<-10	<-100
-----	------	-------

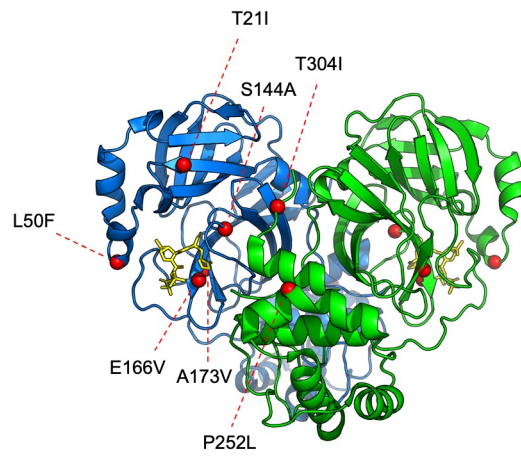


Extended Data Fig. 1

Well	Cleavage site										
	nsp4/5	nsp5/6	nsp6/nsp7	nsp7/nsp8	nsp8/nsp9	nsp9/nsp10	nsp10/nsp12	nsp12/nsp13	nsp13/nsp14	nsp14/nsp15	nsp15/nsp16
WT	TSAVLQ/ SGFRKM	SGVTFQ/ SAVKRT	KVATVQ/ SKMSDV	NRATLQ/ AIASEF	SAVKLQ/ NNELSP	ATVRLQ/ AGNATE	REPMLQ/ SADAQS	PHTVLQ/ AVGACV	NVATLQ/ AENVTG	TFTRLQ/ SLENVA	FYPKLQ/ SSQAWQ
2A1	.	T(P3)I
4C12	.	T(P3)I
2G1	M(P6')I
3H4
4C10	.	T(P3)I
1H2	.	T(P3)I
1H6	.	T(P3)I
3A1
3H8	.	T(P3)I
4G9
1D7
4H3
1A4
5D4
1H4
5H3
4F11
1C6	.	T(P3)I
1E11	.	T(P3)I
2D8	.	T(P3)I
3A8	.	T(P3)I
4F7
1G9
5E11	.	T(P3)I
5D5	.	T(P3)I
2F11	.	T(P3)I
2E11	.	T(P3)I
2G4	.	T(P3)I
1H10	.	T(P3)I	Q(P6')H
4G7	.	T(P3)I
4E10
2A4
5B7	.	T(P3)I
1F2
3E10
2E3	F(P5)C	.	.
1E12
2D9
5A2
4H10
1C1	.	T(P3)I	F(P6)L
2C10	.	T(P3)I
2H11
1B5
5B9
4A6
5E2
4H6	.	T(P3)I
5C10
1B9	.	S(P6)P	R(P6)S
1F7
4E9	.	S(P6)P
3D12

Extended Data Fig. 2

<5% 5-24% 25-49% 50-74% 75-100%

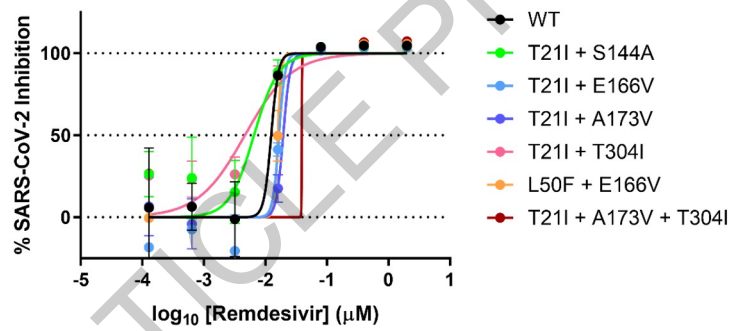
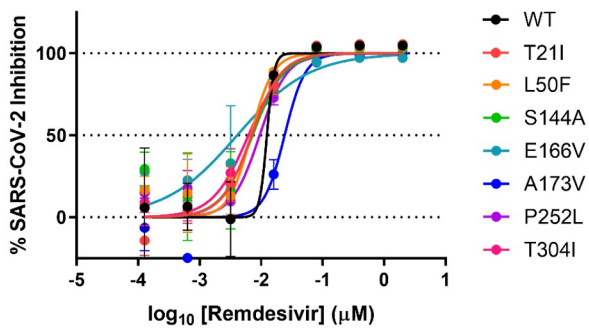
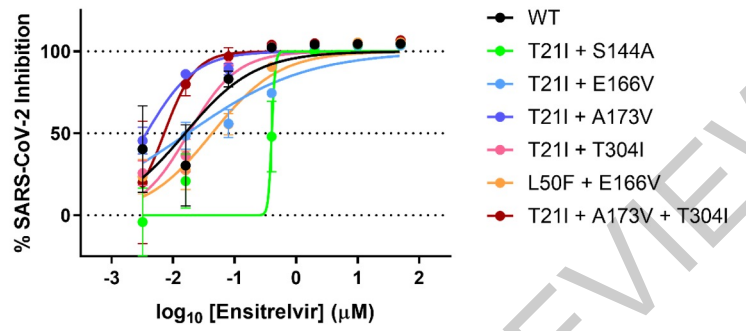
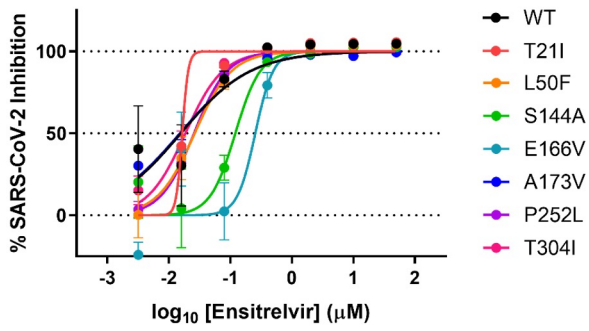


Extended Data Fig. 3

ACCELERATED ARTICLE PREVIEW

IC ₅₀ (μM) ± SD	Nirmatrelvir	Ensitrelvir	Remdesivir
WT	0.051 ± 0.010	0.013 ± 0.005	0.009 ± 0.003
T21I	0.233 ± 0.028	0.021 ± 0.006	0.005 ± 0.002
L50F	0.215 ± 0.108	0.034 ± 0.006	0.007 ± 0.004
S144A	0.024 ± 0.011	0.166 ± 0.039	0.003 ± 0.003
E166V	5.10 ± 4.24	0.294 ± 0.124	0.002 ± 0.001
A173V	0.088 ± 0.027	0.022 ± 0.012	0.017 ± 0.005
P252L	0.297 ± 0.073	0.023 ± 0.009	0.006 ± 0.003
T304I	0.278 ± 0.043	0.019 ± 0.011	0.006 ± 0.002
T21I + S144A	0.478 ± 0.420	0.231 ± 0.148	0.005 ± 0.004
T21I + E166V	4.23 ± 2.90	0.042 ± 0.021	0.021 ± 0.006
T21I + A173V	0.160 ± 0.038	0.006 ± 0.005	0.018 ± 0.001
T21I + T304I	0.168 ± 0.030	0.013 ± 0.004	0.003 ± 0.001
L50F + E166V	2.70 ± 1.53	0.046 ± 0.024	0.017 ± 0.000
T21I + A173V + T304I	0.756 ± 0.391	0.006 ± 0.004	0.025 ± 0.010

Extended Data Fig. 4



Extended Data Fig. 5

ACCELERATED ARTICLE PREVIEW

a

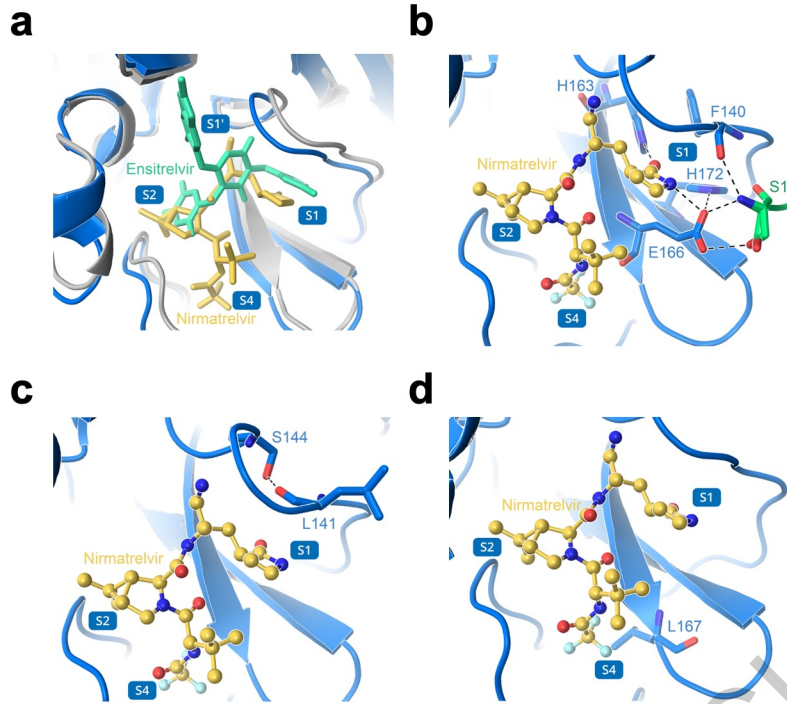
IC ₅₀ (μM)	Nirmatrelvir	Ensitrelvir	Remdesivir
WT	2.128	0.178	3.840
A-P30	60.7	0.383	5.300
B-P30	61.4	0.534	5.010
C-P30	116.3	4.576	4.120

b

Fold change in IC ₅₀ relative to WT	Nirmatrelvir	Ensitrelvir	Remdesivir
A-P30	-28.52	-2.15	-1.38
B-P30	-28.83	-3.00	-1.30
C-P30	-54.65	-25.71	-1.07

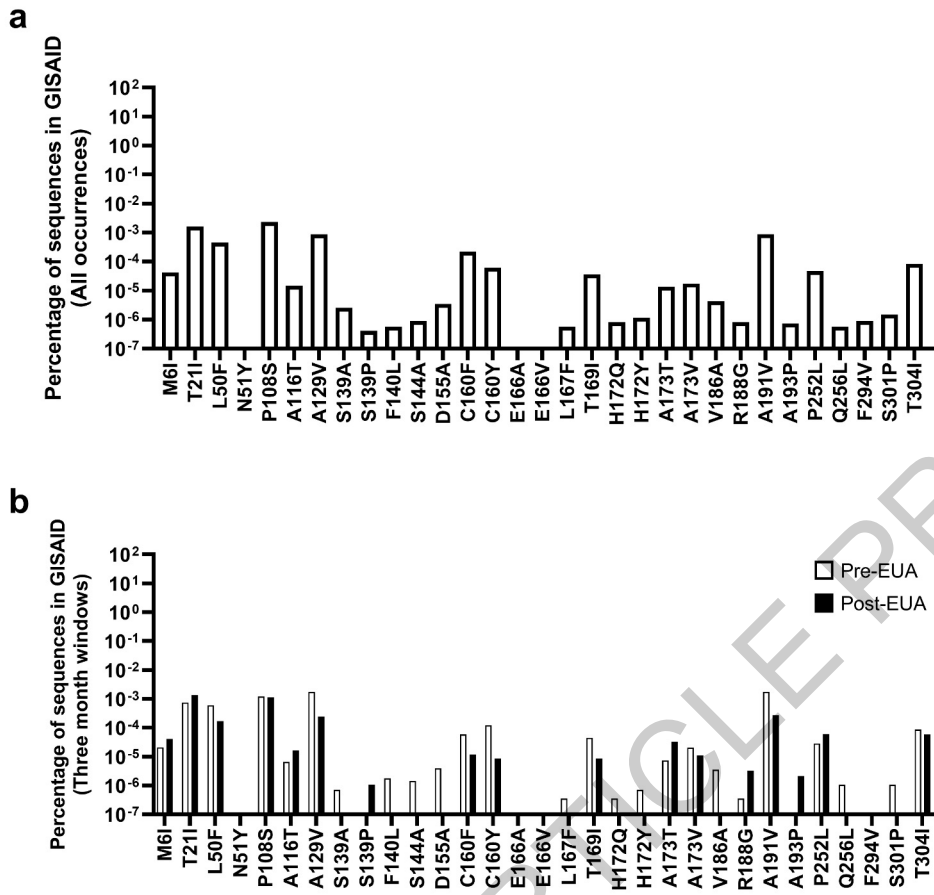
<-5	<-10	<-100
-----	------	-------

Extended Data Fig. 6



Extended Data Fig. 7

ACCELERATED ARTICLE PREVIEW



Extended Data Fig. 8

Reporting Summary

Nature Portfolio wishes to improve the reproducibility of the work that we publish. This form provides structure for consistency and transparency in reporting. For further information on Nature Portfolio policies, see our [Editorial Policies](#) and the [Editorial Policy Checklist](#).

Statistics

For all statistical analyses, confirm that the following items are present in the figure legend, table legend, main text, or Methods section.

- | n/a | Confirmed |
|-------------------------------------|--|
| <input type="checkbox"/> | <input checked="" type="checkbox"/> The exact sample size (n) for each experimental group/condition, given as a discrete number and unit of measurement |
| <input type="checkbox"/> | <input checked="" type="checkbox"/> A statement on whether measurements were taken from distinct samples or whether the same sample was measured repeatedly |
| <input type="checkbox"/> | <input checked="" type="checkbox"/> The statistical test(s) used AND whether they are one- or two-sided
<i>Only common tests should be described solely by name; describe more complex techniques in the Methods section.</i> |
| <input checked="" type="checkbox"/> | <input type="checkbox"/> A description of all covariates tested |
| <input type="checkbox"/> | <input checked="" type="checkbox"/> A description of any assumptions or corrections, such as tests of normality and adjustment for multiple comparisons |
| <input type="checkbox"/> | <input checked="" type="checkbox"/> A full description of the statistical parameters including central tendency (e.g. means) or other basic estimates (e.g. regression coefficient) AND variation (e.g. standard deviation) or associated estimates of uncertainty (e.g. confidence intervals) |
| <input type="checkbox"/> | <input checked="" type="checkbox"/> For null hypothesis testing, the test statistic (e.g. F , t , r) with confidence intervals, effect sizes, degrees of freedom and P value noted
<i>Give P values as exact values whenever suitable.</i> |
| <input checked="" type="checkbox"/> | <input type="checkbox"/> For Bayesian analysis, information on the choice of priors and Markov chain Monte Carlo settings |
| <input checked="" type="checkbox"/> | <input type="checkbox"/> For hierarchical and complex designs, identification of the appropriate level for tests and full reporting of outcomes |
| <input checked="" type="checkbox"/> | <input type="checkbox"/> Estimates of effect sizes (e.g. Cohen's d , Pearson's r), indicating how they were calculated |

Our web collection on [statistics for biologists](#) contains articles on many of the points above.

Software and code

Policy information about [availability of computer code](#)

- | | |
|-----------------|---|
| Data collection | SoftMax Pro 7.0.2 (Molecular Devices, LLC) was used to measure luminescence in the inhibition assays. |
| Data analysis | DeltaGraph version 7 (Red Rock Software) and GraphPad Prism version 9.4 (Dotmatics) were used for determination of IC50 values and statistical tests. GraphPad version 9.4 was used for data visualization. Lasergene software version 17 (DNASTAR) was used for Sanger sequencing analysis. MinKNOW v22.05.1, ONT Epi2Me ARTIC Nextflow pipeline v0.3.16, Pangolin 4.0.6 with USHER v1.6, and V-pipe version 2.99.2 was used for next-generation sequencing analysis. seaborn v0.10.0, which utilizes SciPy, was used for clustering. Geneious Prime v2022.1 with PHYML extension was used for phylogenetic analyses. COVID-19 CG was used for querying sequences deposited to GISAID. CellProfiler version 4.0.7 was used for image analysis. |

For manuscripts utilizing custom algorithms or software that are central to the research but not yet described in published literature, software must be made available to editors and reviewers. We strongly encourage code deposition in a community repository (e.g. GitHub). See the Nature Portfolio [guidelines for submitting code & software](#) for further information.

Data

Policy information about [availability of data](#)

All manuscripts must include a [data availability statement](#). This statement should provide the following information, where applicable:

- Accession codes, unique identifiers, or web links for publicly available datasets
- A description of any restrictions on data availability
- For clinical datasets or third party data, please ensure that the statement adheres to our [policy](#)

All experimental data are provided in the manuscript. The sequences of mutants from passaging in Vero E6 cells have been deposited to GenBank (ON924329-ON924335, ON930401-ON930431). The raw next-generation sequencing data of passaging in Huh7-ACE2 cells are available from the NCBI Short Read Archive under BioProject Accession ID PRJNA852265. The structures of the 3CLpro-nirmatrelvir complex and 3CLpro-ensitrelvir complex were downloaded from PDB under accession codes 7VH8 and 7VU6, respectively. The Wuhan-Hu-1 sequence used for alignment was downloaded from GenBank (accession no. MN908947).

Human research participants

Policy information about [studies involving human research participants and Sex and Gender in Research](#).

Reporting on sex and gender	N/A, this study did not involve human research participants.
Population characteristics	N/A, this study did not involve human research participants.
Recruitment	N/A, this study did not involve human research participants.
Ethics oversight	N/A, this study did not involve human research participants.

Note that full information on the approval of the study protocol must also be provided in the manuscript.

Field-specific reporting

Please select the one below that is the best fit for your research. If you are not sure, read the appropriate sections before making your selection.

- Life sciences Behavioural & social sciences Ecological, evolutionary & environmental sciences

For a reference copy of the document with all sections, see [nature.com/documents/nr-reporting-summary-flat.pdf](https://www.nature.com/documents/nr-reporting-summary-flat.pdf)

Life sciences study design

All studies must disclose on these points even when the disclosure is negative.

Sample size	No sample size calculation was performed. We utilized sample sizes as used in similar studies which allowed for results which could be replicated (e.g., Iketani et al 2022 Nature, Liu et al 2022 Nature, Wang et al 2021 Nature).
Data exclusions	No data were excluded.
Replication	The inhibition assay in Fig. 2b and the growth assay in Fig. 3b were repeated independently twice. The inhibition assay in Fig. 4a were repeated independently three times.
Randomization	As this is an observational study, randomization is not relevant.
Blinding	As this is an observational study, investigators were not blinded.

Reporting for specific materials, systems and methods

We require information from authors about some types of materials, experimental systems and methods used in many studies. Here, indicate whether each material, system or method listed is relevant to your study. If you are not sure if a list item applies to your research, read the appropriate section before selecting a response.

Materials & experimental systems

- n/a | Involved in the study
- Antibodies
- Eukaryotic cell lines
- Palaeontology and archaeology
- Animals and other organisms
- Clinical data
- Dual use research of concern

Methods

- n/a | Involved in the study
- ChIP-seq
- Flow cytometry
- MRI-based neuroimaging

Eukaryotic cell lines

Policy information about [cell lines and Sex and Gender in Research](#)

Cell line source(s)	Vero E6 cells were obtained from ATCC (Catalog #CRL-1586), HEK293T cells were obtained from ATCC (Catalog #CRL-3216), and Vero E6-TMPRSS2-T2A-ACE2 cells were obtained from BEI Resources (Catalog #NR-54970). Huh7-ACE2 cells were generated previously (refs 33,40).
Authentication	Cell lines were purchased from authenticated vendors, and morphology was also confirmed visually prior to use.
Mycoplasma contamination	Cell lines tested mycoplasma negative.
Commonly misidentified lines (See ICLAC register)	No commonly misidentified cell lines were used in this study.

Dual use research of concern

Policy information about [dual use research of concern](#)

Hazards

Could the accidental, deliberate or reckless misuse of agents or technologies generated in the work, or the application of information presented in the manuscript, pose a threat to:

- | No | Yes |
|-------------------------------------|---|
| <input checked="" type="checkbox"/> | <input type="checkbox"/> Public health |
| <input checked="" type="checkbox"/> | <input type="checkbox"/> National security |
| <input checked="" type="checkbox"/> | <input type="checkbox"/> Crops and/or livestock |
| <input checked="" type="checkbox"/> | <input type="checkbox"/> Ecosystems |
| <input checked="" type="checkbox"/> | <input type="checkbox"/> Any other significant area |

Experiments of concern

Does the work involve any of these experiments of concern:

- | No | Yes |
|-------------------------------------|---|
| <input checked="" type="checkbox"/> | <input type="checkbox"/> Demonstrate how to render a vaccine ineffective |
| <input type="checkbox"/> | <input checked="" type="checkbox"/> Confer resistance to therapeutically useful antibiotics or antiviral agents |
| <input checked="" type="checkbox"/> | <input type="checkbox"/> Enhance the virulence of a pathogen or render a nonpathogen virulent |
| <input checked="" type="checkbox"/> | <input type="checkbox"/> Increase transmissibility of a pathogen |
| <input checked="" type="checkbox"/> | <input type="checkbox"/> Alter the host range of a pathogen |
| <input checked="" type="checkbox"/> | <input type="checkbox"/> Enable evasion of diagnostic/detection modalities |
| <input checked="" type="checkbox"/> | <input type="checkbox"/> Enable the weaponization of a biological agent or toxin |
| <input checked="" type="checkbox"/> | <input type="checkbox"/> Any other potentially harmful combination of experiments and agents |

Precautions and benefits

Biosecurity precautions	All experiments were conducted in a Biosafety Level 3 (BSL-3) facility.
Biosecurity oversight	Prior to conducting this work, the protocol was reviewed and approved by Columbia University's Institutional Biosafety Committee (IBC).
Benefits	Understanding of the mutations that confer nirmatrelvir resistance, as well as the mechanisms by which SARS-CoV-2 acquires such resistance, is critical for clinical surveillance of nirmatrelvir resistance and for the development of future protease inhibitors.

Communication benefits

Communication of these results will allow for clinical surveillance and appropriate use of nirmatrelvir, as well as provide insight into development of the next generation of protease inhibitors. Some of these mutant viruses have already been described elsewhere. Furthermore, as these described viruses remain susceptible to other therapeutic agents and arose naturally, we believe that communication of our data outweigh the risks.